PCCP

ROYAL SOCIETY OF CHEMISTRY

PAPER

View Article Online
View Journal

Cite this: DOI: 10.1039/d5cp04913j

Halogen-driven magnetic properties of two-dimensional binary and Janus Cr_2XYSe_2 (X, Y = F, Cl, Br, I) monolayers

S. Davoudi Tanha, [a] Y. Mogulkoc *[a] and A. Mogulkoc [b]

In this study, we investigate the structural, electronic, and magnetic properties of the orthorhombic phase of Cr_2XYSe_2 (X, Y = F, Cl, Br, I) two-dimensional monolayers using first-principles calculations based on density functional theory. The calculated exchange interaction parameters and magnetic anisotropies exhibit a strong dependence on both the chemical composition of the monolayers and the Hubbard parameter *U*. This finding indicates that the interplay between spin–orbit coupling and electron localization is crucial for stabilizing long-range magnetic order in these systems. Furthermore, the renormalized magnon spectrum derived from our calculations yields Curie temperatures of approximately 200 K for the iodine-based monolayers, the highest among the compositions studied, indicating the maximum thermal stability. The results of this investigation provide a comprehensive understanding of how chemical substitution, electron correlations, and symmetry reduction interact to control magnetism in two-dimensional materials. This study advances the understanding of magnetism in Cr_2XYSe_2 monolayers and establishes a distinct materials design framework for two-dimensional van der Waals magnetic systems.

Received 17th December 2025,
Accepted 27th March 2026

DOI: 10.1039/d5cp04913j

rsc.li/pccp

I. Introduction

The discovery of intrinsic long-range magnetic order in intrinsic 2D ferromagnets such as CrI_3 and $Cr_2Ge_2Te_6$ has established two-dimensional (2D) magnets as promising candidates for investigating spin-dependent phenomena in reduced dimensionality.[1–8] In these systems, magnetic anisotropy plays a critical role in stabilizing finite-temperature magnetic order by lifting the spin-rotational symmetry of the isotropic Heisenberg model, which results in a finite magnon gap that suppresses long-wavelength spin fluctuations, thereby enabling long-range magnetic order at finite temperature.[1–3,9–12]

Recently, 2D van der Waals Cr–halogenide–chalcogenide, CrXY (X = F, Cl, Br, I; Y = S, Se) monolayers, typically characterized by hexagonal and triangular lattices, have been extensively investigated due to their distinctive magnetic and electronic properties in both theoretical and experimental studies.[13–24] Beyond high-symmetry lattices, orthorhombic structures lack three- or sixfold rotational symmetry and possess two inequivalent in-plane crystallographic directions, leading to distinct magnetic behavior and more complex spin and electronic phenomena.[15–17,25–28] In these systems, substituting the top-layer chalcogen with a halogen of different electronegativity further lowers the symmetry and modifies the exchange interactions, thereby tuning the electronic structure and magnetic properties.[29]

Additionally, considerable studies have been conducted to obtain CrXY monolayers with higher anisotropy energy and transition temperature.[17–24] The Curie temperature of the CrXY monolayer can be enhanced using various strategies, such as applying strain to 2D CrSBr,[30] replacing Cr atoms with other transition atoms in the CrSI monolayer,[19,20] or chemical doping in CrSBr.[21] Furthermore, the low-symmetry Cr–halogenide–chalcogenide monolayer, belonging to the orthorhombic *Pmmn* space group, has been identified as a 2D long-range magnetic material through both experimental observations and theoretical calculations.[8,15,17,31–33] The rectangular-phase CrSBr monolayer was synthesized using a modified chemical vapor transport technique, revealing A-type antiferromagnetic order with a Néel temperature of approximately 132 K.[8] Subsequent research has demonstrated that 2D van der Waals CrSBr, fabricated through mechanically exfoliated flakes, exhibits stability in the orthorhombic structure, accompanied by notable in-plane anisotropy.[31] From the results of this study, bulk and few-layer orthorhombic-CrSBr exhibit A-type antiferromagnetic order below approximately 132 K. In contrast, its monolayer counterpart exhibits intraplanar ferromagnetic order,

[a] Department of Physics Engineering, Faculty of Engineering, Ankara University, Ankara, 06100, Turkey. E-mail: mogulkoc@eng.ankara.edu.tr
[b] Department of Physics, Faculty of Science, Ankara University, Ankara, 06100, Turkey

with a transition temperature of approximately 145 K. A recent experimental investigation has reported the emergence of in-plane ferromagnetic order in monolayer CrSBr, with a Curie temperature of $T_C \approx 146$ K.[15] As reported in a theoretical study, the CrSI monolayer, which stabilized in the orthorhombic structure, exhibits in-plane ferromagnetism with a magnetic anisotropy energy of approximately 0.52 meV.[17]

In transition-metal (TM) compounds, the presence of partially filled d-orbitals makes it essential to include on-site Coulomb interactions, represented by the Hubbard parameter. The overlap between atomic orbitals partially screens the local d-electron repulsion, which in turn strongly influences the electronic and magnetic properties of TM monolayers.[32,33] The magnetic behavior of CrSBr monolayers can be strongly influenced by correlation effects, which are characterized by the Hubbard parameter U.[16,34] A theoretical study has shown that, in the orthorhombic CrSBr monolayer, both the Heisenberg exchange parameters and the magnetic anisotropy depend on the Hubbard parameter.[16] The dependence of the magnetic parameters on U results in transition temperatures ranging from approximately $\sim$100 to 140 K for U values between 0 and 4 eV. A recent theoretical study of the orthorhombic CrSBr monolayer reports an intralayer ferromagnetic ground state with a transition temperature of approximately 145 K.[35]

In this work, we investigate ten binary and Janus Cr_2XYSe_2 (X, Y = F, Cl, Br, I) monolayers *via* halogen substitution on the Cr–Se lattice, focusing on the orthorhombic phase, in which reduced symmetry introduces two inequivalent in-plane directions. Using DFT+U to account for electronic correlation in the Cr 3d orbitals and an anisotropic Heisenberg model combined with linear spin-wave theory, we establish how structural asymmetry and halogen chemistry modulate exchange interactions, magnetic anisotropy, and the easy-axis orientation. In particular, the Cr_2XYSe_2 family consists of orthorhombic 2D monolayers with tunable chalcogen and halogen atoms. However, how these substitutions, together with on-site electronic correlation, affect their magnetic properties remains to be comprehensively investigated. In this study, we clarify these effects and describe magnetism in this material family, offering a practical theoretical basis for the development of Cr-based magnetic and functional materials.

II. Model and method

A. First-principles calculations

Investigations of the electronic and magnetic properties of 2D Cr_2XYSe_2 were carried out using first-principles calculations based on density functional theory (DFT) with the projector augmented-wave (PAW) method,[36,37] as implemented in the Vienna *ab initio* simulation package.[38,39] The Perdew–Burke–Ernzerhof (PBE) formulation within the generalized gradient approximation (GGA) was employed for the exchange–correlation functional.[40] The DFT+U method was used to account for the strongly correlated 3d electrons of Cr atoms.[41,42] We considered Hubbard U values in the range 0–4 eV to evaluate the influence of on-site Coulomb interactions on the physical properties of Cr_2XYSe_2 monolayers. Within the DFT+U framework, the Hubbard U parameter represents the effective screened on-site Coulomb interaction of localized Cr 3d electrons rather than a directly tunable experimental variable, and its systematic variation is employed as a controlled theoretical approach to examine the influence of correlation strength—partially capturing changes in electronic screening induced by external environments such as dielectric substrates (*e.g.*, hexagonal BN) or encapsulation—on the magnetic properties of Cr_2XYSe_2 monolayers. Additionally, the Heyd–Scuseria–Ernzerhof (HSE06) screened hybrid functional is employed to assess the appropriate value of the Hubbard parameter.[43,44] The plane-wave cutoff energy was set to 700 eV. For Brillouin zone (BZ) integration, a $16 \times 16 \times 1$ Monkhorst–Pack k-point mesh[45] was utilized. A vacuum thickness of 30 Å was introduced to avoid spurious interactions between periodic layers along the z direction. The atomic positions and lattice parameters were relaxed using the conjugate-gradient method until the residual forces on each atom were less than 0.001 eV Å^{-1}, with an energy convergence criterion of 10^{-10} eV between successive electronic steps. To investigate the dynamical stability of the optimized structures, phonon dispersion calculations were performed for all ten chemical compositions of Cr_2XYSe_2. For this purpose, density functional perturbation theory (DFPT) calculations were carried out using the Phonopy code,[46] employing a $5 \times 5 \times 1$ supercell. The thermodynamic stability of Cr_2XYSe_2 monolayers was investigated by using *ab initio* molecular dynamics (AIMD) simulations. The system has been regarded as a canonical ensemble (NVT), with a $4 \times 4 \times 1$ supercell and the Andersen thermostat.[47] The temperature was set to be in the range of 110–180 K, depending on the calculated transition temperatures of the different chemical compositions, with a time step of 2 fs.

B. Anisotropic Heisenberg model and spin-wave excitations

Magnetic anisotropy plays a crucial role in stabilizing long-range magnetic order in 2D materials. In Sections II.B.1 and II.B.2, the anisotropic Heisenberg Hamiltonian was introduced for out-of-plane and in-plane magnetic configurations, respectively. The Curie temperature of two-dimensional ferromagnets is sensitive to magnetic anisotropy, which originates from spin–orbit coupling. Different theoretical approaches used to solve the Heisenberg Hamiltonian treat anisotropies at different levels of approximation, including Monte Carlo simulations, Green's function methods, and spin-wave theories. Consequently, the predicted Curie temperatures may vary depending on the computational framework employed.[2,48–50] As reported in ref. 51 and 52, the Monte Carlo and Green's function methods overestimate the Curie temperature compared to the spin-wave method. They also found that for $CrCl_3$, which has low magnetic anisotropy, the renormalized spin-wave and Green's function methods provide a more accurate estimation of the Curie temperature. To consider the thermal stability of the magnetic ground state, linear spin-wave theory was employed. For this purpose, the Holstein–Primakoff (HP)

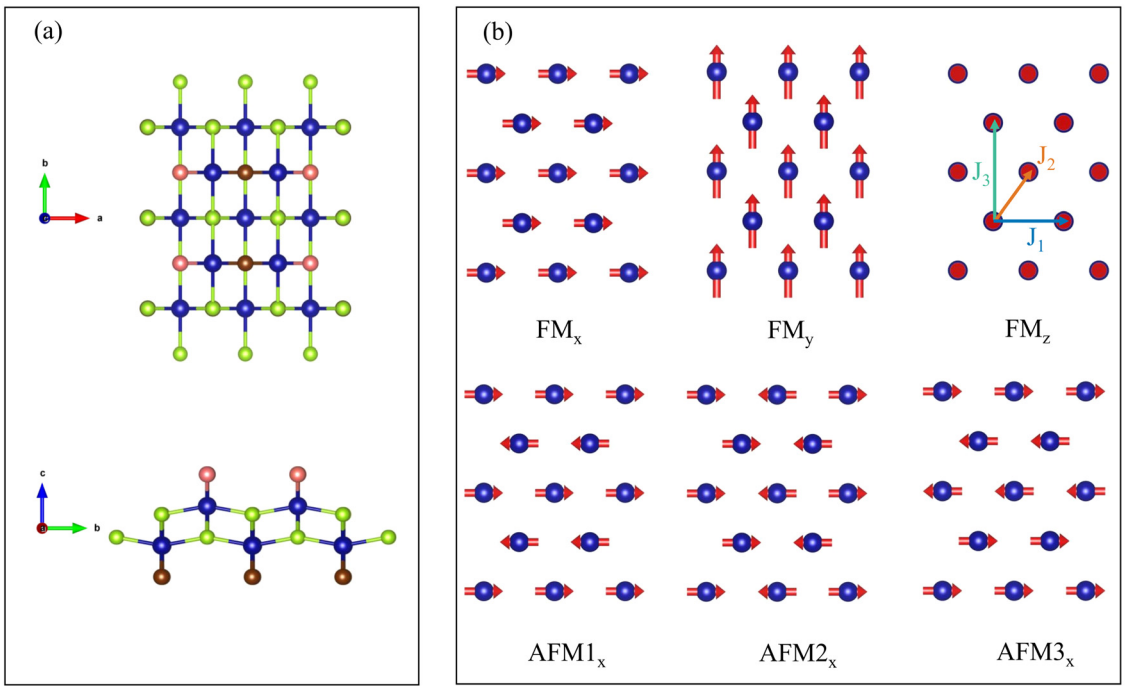

Fig. 1 (a) Atomic structure of the Cr_2XYSe_2 monolayers in the orthorhombic phase, shown in the top and side views, with a and b indicating the lattice vectors. Blue and green colors represent Cr and Se atoms, and purple and brown ones denote the halogen atoms, X and Y. (b) Spin configurations employed to determine the magnetic parameters, including ferromagnetic alignments FM_x, FM_y, and FM_z, and antiferromagnetic configurations $AFM1_x$, $AFM2_x$, and $AFM3_x$. (Configurations with spins aligned along z for AFM states are provided in Fig. S2 of the SI.) The three exchange interactions J_1, J_2, and J_3 correspond to the first, second, and third nearest Cr–Cr pairs.

transformation was applied to map the spin Hamiltonian onto a bosonic representation.[2,50] Assuming a low magnon population, the first-order HP approximation is employed. In the following, we analytically derive the magnetic parameters and the associated magnon dispersions, enabling us to predict how the magnetic behavior varies with chemical composition and the strength of the on-site Coulomb interaction. To investigate the temperature dependence of magnetization, the magnon energy is renormalized using mean-field theory, as discussed in Section II.B.3.

1. Out-of-plane anisotropic Hamiltonian. The Hamiltonian for the anisotropic Heisenberg model for out-of-plane magnets can be written as

$$H = -\sum_{\tau=1}^{3} J_\tau \sum_{\langle ij\rangle_\tau} \mathbf{S}_i \cdot \mathbf{S}_j - A \sum_i \left(S_i^z\right)^2 \qquad (1)$$

with $\mathbf{S}_i$ and $\mathbf{S}_j$ denoting the spin operators associated with the atomic lattice sites i and j, respectively, as shown in Fig. 1. In the orthorhombic phase configuration with lattice constants a and b (Table 1), three Cr–Cr interaction bonds are included, as each Cr atom is surrounded by two others in the first, four in the second, and two in the third nearest neighbors. Accordingly, in eqn (1), the Heisenberg exchange parameter J_τ is defined as, J_1 corresponds to the first-nearest-neighbor bonds, $\langle ij\rangle_1$, of length a, while J_2 describes the second-nearest-neighbor bonds, $\langle ij\rangle_2$, of length $\sqrt{a^2+b^2}$, connecting sites on the two different sublattices. The third-nearest-neighbor coupling, denoted by J_3, $\langle ij\rangle_3$, connects the sites separated by the lattice constant b. The second term of the Hamiltonian describes the single-ion magnetic anisotropy. For the van der Waals magnetic monolayer with uniaxial anisotropy, the sign of A determines

Table 1 Calculated in-plane lattice constants a and b (Å) as a function of the Hubbard parameter U (eV) for binary and Janus Cr_2XYSe_2 monolayers

	Lattice constant (Å)	U = 0	U = 1	U = 2	U = 3	U = 4
$Cr_2F_2Se_2$	a	3.30	3.31	3.31	3.31	3.26
	b	5.09	5.11	5.14	5.19	5.28
$Cr_2Cl_2Se_2$	a	3.53	3.55	3.56	3.57	3.58
	b	5.05	5.08	5.11	5.15	5.18
$Cr_2Br_2Se_2$	a	3.64	3.65	3.66	3.68	3.69
	b	5.04	5.06	5.10	5.13	5.16
$Cr_2I_2Se_2$	a	3.80	3.81	3.83	3.84	3.86
	b	5.01	5.04	5.08	5.11	5.15
Cr_2BrFSe_2	a	3.46	3.47	3.48	3.48	3.80
	b	5.05	5.08	5.11	5.15	5.19
$Cr_2BrClSe_2$	a	3.58	3.60	3.61	3.62	3.63
	b	5.04	5.07	5.10	5.14	5.17
Cr_2ClISe_2	a	3.66	3.68	3.69	3.70	3.70
	b	5.03	5.06	5.10	5.13	5.17
Cr_2BrISe_2	a	3.72	3.73	3.74	3.76	3.77
	b	5.02	5.05	5.08	5.12	5.16

the preferred orientation of the magnetic moments, where the positive and negative signs correspond to out-of-plane and in-plane easy axes of magnetization, respectively. Given that Cr_2XYSe_2 monolayers exhibit both out-of-plane and in-plane magnetic anisotropy depending on the chemical composition and the Hubbard parameter, the in-plane form of the Hamiltonian will be discussed in Section II.B.2. To derive the magnetic parameters of the Hamiltonian in eqn (1), four distinct magnetic states, one FM and three AFM, as illustrated in Fig. 1, are considered. By rewriting the Hamiltonian for each configuration and substituting the corresponding spin-orientation energies, the exchange and anisotropy parameters can be determined, as detailed in the SI.

The first-order HP transformation[50] for the orthorhombic lattice with the out-of-plane easy axis of magnetization can be written as

$$\begin{aligned} S_i^+ &= \sqrt{2S}a_i, \\ S_i^- &= \sqrt{2S}a_i^\dagger, \\ S_i^z &= S - a_i^\dagger a_i, \end{aligned} \tag{2}$$

for the sublattice in the a direction, and

$$\begin{aligned} S_i^+ &= \sqrt{2S}b_i, \\ S_i^- &= \sqrt{2S}b_i^\dagger, \\ S_i^z &= S - b_i^\dagger b_i. \end{aligned} \tag{3}$$

for the sublattice in the b direction (a and b directions shown in Fig. 1). Here, S is the total spin moment (in units of $\hbar$), and a_i, $a_i^\dagger$, and b_i, $b_i^\dagger$ are the creation and annihilation operators in different sublattices that obey the bosonic commutation relations. Ladder spin operators are defined as $S_i^\pm = S_i^x \pm iS_i^y$. To obtain the Hamiltonian in momentum space, the Fourier transformation is applied, $a_i = \frac{1}{\sqrt{N}}\sum_{\mathbf{k}} e^{i\mathbf{k}\cdot\mathbf{r}_i}a_k$. As a result, the Hamiltonian in reciprocal space

$$H = \sum_{\mathbf{k}} \begin{pmatrix} a_{\mathbf{k}}^\dagger & b_{\mathbf{k}}^\dagger \end{pmatrix} H(\mathbf{k}) \begin{pmatrix} a_{\mathbf{k}} \\ b_{\mathbf{k}} \end{pmatrix} \tag{4}$$

where

$$H(\mathbf{k}) = \begin{pmatrix} A_{\mathbf{k}} & B_{\mathbf{k}} \\ B_{\mathbf{k}} & A_{\mathbf{k}} \end{pmatrix} \tag{5}$$

In eqn (5), the matrix indexes are

$$\begin{aligned} A_{\mathbf{k}} &= 2S\left[(J_1(\mathbf{0}) - J_1(\mathbf{k})) + (J_3(\mathbf{0}) - J_3(\mathbf{k})) + J_2(\mathbf{k}) + \frac{A}{2}\right], \\ B_{\mathbf{k}} &= -2SJ_2(\mathbf{k}). \end{aligned} \tag{6}$$

In the above equation,

$$J_\tau(\mathbf{k}) = \sum_{\tau=1}^{3} J_\tau \cos(\mathbf{k}\cdot\Delta\mathbf{R})_\tau, \tag{7}$$

$\cos(\mathbf{k}\cdot\Delta\mathbf{R})_\tau$ is the structure factor for the first, second, and third nearest neighbors of Cr atoms, and $\Delta\mathbf{R}$ is the vector that connects the nearest neighbors.

$$\begin{aligned} \cos(\mathbf{k}\cdot\Delta\mathbf{R})_{\langle ij\rangle_1} &= 4\cos(k_x a), \\ \cos(\mathbf{k}\cdot\Delta\mathbf{R})_{\langle ij\rangle_2} &= 8\cos\left(\frac{k_x a}{2}\right)\cos\left(\frac{k_y b}{2}\right), \\ \cos(\mathbf{k}\cdot\Delta\mathbf{R})_{\langle ij\rangle_3} &= 4\cos(k_y b). \end{aligned} \tag{8}$$

In the equation, all structure factors are multiplied by two, as there are two Cr atoms in the unit cell. The eigenvalues of the Hamiltonian in eqn (5) can be derived as

$$\omega_{\mathbf{k}}^\pm = A_{\mathbf{k}} \pm B_{\mathbf{k}} \tag{9}$$

where $\omega_{\mathbf{k}}^+$ and $\omega_{\mathbf{k}}^-$ belong to the acoustic and optical magnon branches, respectively. More details of the derivation are available in the SI. The magnon energy gap in $\mathbf{k} \to 0$ for the acoustic branch is derived as $AS/2$. As a result, the magnon gap around the Γ point in the BZ strongly depends on the single-ion anisotropy. Although this anisotropy is small in magnitude, it plays a crucial role in opening a finite magnon gap and ensuring nonzero magnetization at finite temperature.[53]

2. In-plane anisotropic Hamiltonian. In 2D magnets with an in-plane easy axis, the inter-site magnetic anisotropy within the $\alpha\beta$ plane becomes crucial. Accordingly, the anisotropic Heisenberg Hamiltonian can be written as

$$\begin{aligned} H = &-\sum_{\tau=1}^{3} J_\tau \sum_{\langle ij\rangle_\tau} \mathbf{S}_i \cdot \mathbf{S}_j - A\sum_i (\mathbf{S}_i \cdot \boldsymbol{\mu})^2 \\ &- \delta \sum_{\langle ij\rangle_1} \left(S_i^\alpha S_j^\alpha - S_i^\beta S_j^\beta\right) \end{aligned} \tag{10}$$

Here, the first two terms of the Hamiltonian are the same as those in eqn (1). The indices α, β denote the directions within the easy plane of magnetization and μ denote the axis normal to this plane in the Cartesian basis (x, y, z). The last terms in eqn (10) belong to the inter-site magnetic anisotropy within the easy plane of magnetization, $\alpha\beta$-plane. Given that the magnitude of δ is relatively small, it is sufficient to include only the sites closest to the first neighbor ($\langle ij\rangle_1$). Taking into account the four different spin orientations (Fig. 1), the magnetic parameters of 2D Cr_2XYSe_2 for all possible in-plane easy axes α and β are derived, as reported in the SI.

For in-plane magnets, the HP transformations can be written for the sublattice in the a direction as

$$\begin{aligned} S_i^+ &= \sqrt{2S}a_i^\dagger, \\ S_i^- &= \sqrt{2S}a_i, \\ S_i^{\alpha,\beta} &= a_i^\dagger a_i - S, \end{aligned} \tag{11}$$

and for the sublattice in the b direction as

$$S_i^+ = \sqrt{2S}b_i^\dagger,$$
$$S_i^- = \sqrt{2S}b_i, \quad (12)$$
$$S_i^{\alpha,\beta} = b_i^\dagger b_i - S.$$

The conventional spin ladder operators are given by $S_i^\pm = -S_i^\mu \pm iS_i^{\alpha,\beta}$. By applying the HP transformation to the Hamiltonian in eqn (1) and subsequently transforming to momentum space using the Fourier transformation,

$$H = \sum_{\mathbf{k}} \left(a_{\mathbf{k}}^\dagger\ b_{\mathbf{k}}^\dagger\ a_{-\mathbf{k}}\ b_{-\mathbf{k}}\right) H(\mathbf{k}) \begin{pmatrix} a_{\mathbf{k}} \\ b_{\mathbf{k}} \\ a_{-\mathbf{k}}^\dagger \\ b_{-\mathbf{k}}^\dagger \end{pmatrix} \quad (13)$$

where

$$H(\mathbf{k}) = \frac{1}{2}\begin{pmatrix} A_{\mathbf{k}} & -B_{\mathbf{k}} & C_{\mathbf{k}} & 0 \\ -B_{\mathbf{k}} & A_{\mathbf{k}} & 0 & C_{\mathbf{k}} \\ C_{\mathbf{k}} & 0 & -A_{\mathbf{k}} & B_{\mathbf{k}} \\ 0 & C_{\mathbf{k}} & B_{\mathbf{k}} & -A_{\mathbf{k}} \end{pmatrix} \quad (14)$$

and

$$\begin{aligned} A_{\mathbf{k}} &= 2S\Big[(J_1(\mathbf{0}) - J_1(\mathbf{k})) + (J_3(\mathbf{0}) - J_3(\mathbf{k})). \\ &\quad + J_2(\mathbf{0}) - \frac{A}{2} + \left(\delta(\mathbf{0}) + \frac{\delta(\mathbf{k})}{2}\right)\Big], \\ B_{\mathbf{k}} &= -2SJ_2(\mathbf{k}), \\ C_{\mathbf{k}} &= -\frac{S}{2}(\delta(\mathbf{k}) + A) \end{aligned} \quad (15)$$

We can explicitly write

$$J_\tau(\mathbf{k}) = \sum_{\tau=1}^{3} J_\tau \cos(\mathbf{k}\cdot\Delta\mathbf{R})_\tau,$$
$$\delta(\mathbf{k}) = \delta\cos(\mathbf{k}\cdot\Delta\mathbf{R})_{\langle ij\rangle_1} \quad (16)$$

In the above equation, the structure factor, $\cos(\mathbf{k}\cdot\Delta\mathbf{R})_\tau$, is defined in eqn (8), and the corresponding expressions for the exchange parameters and anisotropy energies are provided in the SI. By solving the Hamiltonian of eqn (14), the magnon dispersion can be written as

$$\omega_{\mathbf{k}}^\pm = \sqrt{(A_{\mathbf{k}} \pm B_{\mathbf{k}})^2 - 4C_{\mathbf{k}}{}^2} \quad (17)$$

The spin-wave gap around zero momentum can be derived for the acoustic band as $S\sqrt{8\delta(\delta - A)}$. Here, the presence of the δ term is particularly critical for establishing a long-range magnetic order in 2D monolayers.[11,54–56]

3. Magnetization renormalization due to magnon excitations. According to eqn (5) and (17), the magnon dispersion does not yet include the effect of temperature. To account for thermal effects, the magnon energy should be renormalized. For this purpose, using mean-field theory, the dependence of the number of excited magnons on temperature is investigated.[57] Since each magnon carries one unit of angular momentum, thermal effects lead to its excitation. This reduces the total spin of the system from S to $S - \langle n\rangle$, where n is the number operator that defines the number of magnons at each temperature. The renormalized magnon energy as a function of temperature is given by

$$\omega_{\mathbf{k}}^T = \omega_{\mathbf{k}}^0\left(\frac{S - \langle n\rangle}{S}\right),$$
$$\omega_{\mathbf{k}}^T = \omega_{\mathbf{k}}^0\frac{M(T)}{M_{\text{sat}}}, \quad (18)$$

Here, $M(T)$ and M_{sat} are the temperature-dependent magnetization function and the saturation magnetization, respectively. Employing the Bose–Einstein distribution, $M(T)$ can be formulated as

$$\frac{M(T)}{M_{\text{sat}}} = 1 - \frac{1}{S}\sum_{\mathbf{k}} \frac{1}{\exp\left(\beta\omega_{\mathbf{k}}^0\frac{M(T)}{M_{\text{sat}}}\right) - 1}, \quad (19)$$

$\beta = 1/k_B T$ and k_B is the Boltzmann constant. Eqn (19) is solved iteratively by initially setting $M(T) = M_{\text{sat}}$ and updating $M(T)$ until convergence is reached. Finally, the Curie temperature is defined as the temperature at which the magnetization reaches $M(T) = M_{\text{sat}}/2$.

III. Results and discussion

A. Structural and electronic properties

To study the dynamical stability of the ten possible binary and Janus Cr_2XYSe_2 (X, Y = F, Cl, Br, I) monolayers in the orthorhombic structure with the space group *Pmmn*, DFPT phonon calculations were carried out along the high-symmetry path X → S → Y → Γ → S in the Brillouin zone. As shown in the SI, eight out of the ten considered compositions show no imaginary phonon modes, confirming their dynamical stability. On the other hand, the Cr_2FClSe_2 and Cr_2FISe_2 monolayers display imaginary phonon branches and are therefore dynamically unstable in the orthorhombic phase. In the subsequent sections, we conduct a thorough investigation into the electronic and magnetic properties of the eight stable compounds, which encompass the four binary systems denoted as $Cr_2F_2Se_2$, $Cr_2Cl_2Se_2$, $Cr_2Br_2Se_2$, and $Cr_2I_2Se_2$, and the four Janus monolayers Cr_2BrFSe_2, $Cr_2BrClSe_2$, Cr_2ClISe_2, and Cr_2BrISe_2.

The structural parameters are summarized in Table 1, where a and b denote the lattice constants along the crystallographic a and b axes, respectively, as shown in Fig. 1. For all chemical compositions, both a and b increase with U, except in $Cr_2F_2Se_2$, where a remains almost unchanged and decreases slightly at U = 4 eV. The Cr–Cr distances for the first-, second-, and third-nearest neighbors are reported in the SI. One can see that the lattice constants and Cr–Cr distances follow the same trend, as is well established from periodic trends, the electronegativity decreases from F to I ($\chi_F > \chi_{Cl} > \chi_{Br} > \chi_I$), whereas the atomic radius increases ($r_F < r_{Cl} < r_{Br} < r_I$).[58,59] Consequently, in the binary systems, the relevant structural parameters increase systematically from $Cr_2F_2Se_2$ to $Cr_2I_2Se_2$, while in the Janus systems, they increase from Cr_2BrFSe_2 to Cr_2BrISe_2.

Additionally, the effect of halogen electronegativity is reflected in the charge redistribution, as confirmed by the Bader charge analysis. As the electronegativity decreases from F to I, the charge transferred from Cr to the halogen atoms decreases,

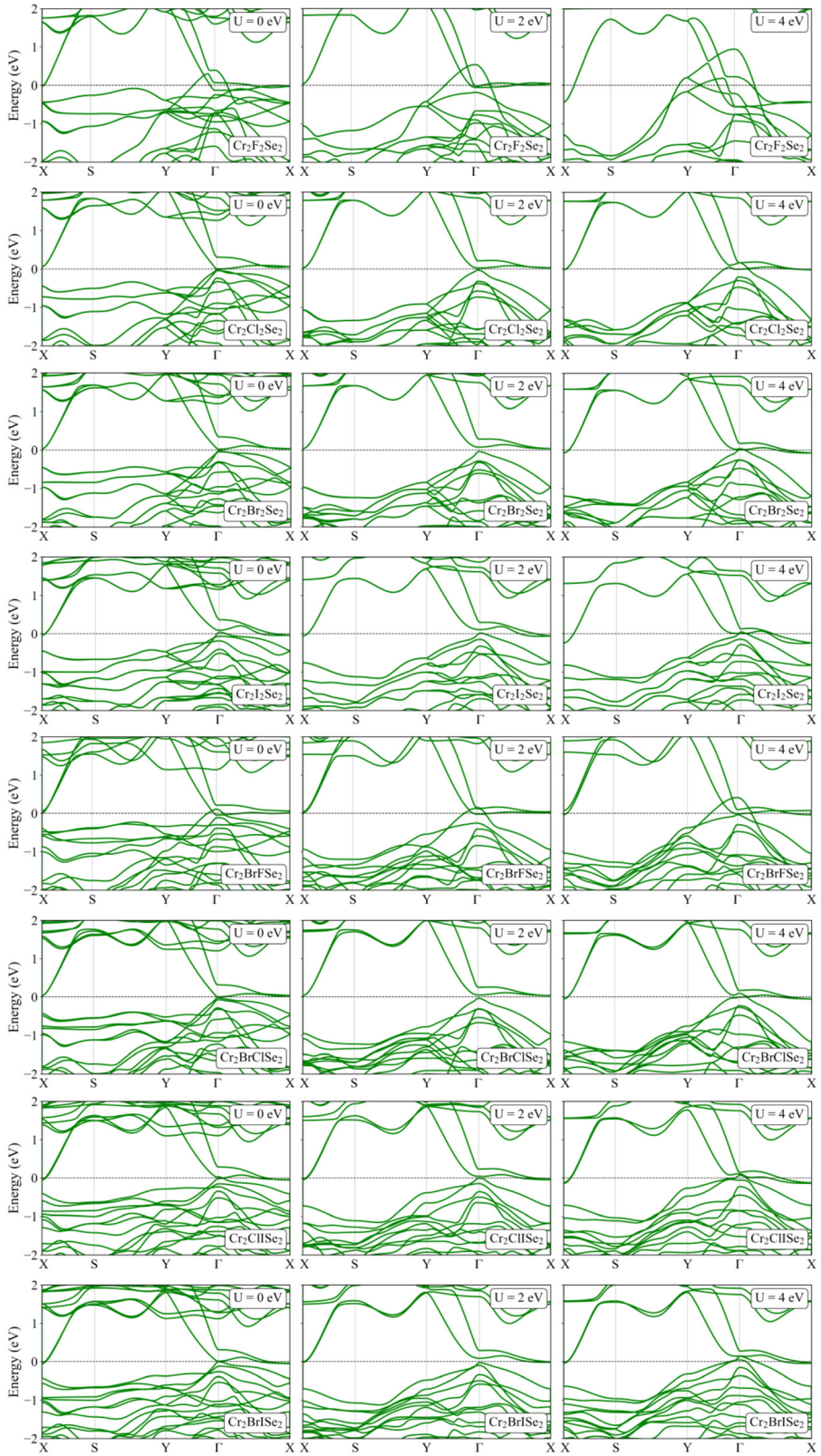

Fig. 2 Electronic band structure in the presence of SOC for U = 0, 2, and 4 eV in 2D Cr_2XYSe_2.

indicating a gradual reduction in bond ionicity (see Tables III and IV in the SI).

Spin-polarized band structures at U = 0, 2, and 4 eV, as shown in Fig. S2 of the SI, reveal systematic trends across the Cr_2XYSe_2 family. The binary monolayers are semimetallic at U = 0 and 2 eV and become metallic at U = 4 eV as electronic correlations increase the band overlap. The Janus monolayers exhibit weak half-metallicity at $U < 3$ eV, arising from the broken mirror symmetry that opens a minority-spin gap. In contrast, this gap vanishes at U = 4 eV, and all Janus structures become metallic. Among all compositions, the F-containing compositions remain metallic for all U, consistent with stronger Cr–F hybridization. As presented in Fig. 2, SOC produces only minor modifications to the band dispersions and does not change the electronic classifications obtained from the collinear calculations. Moreover, the PBE and HSE06 band structures for the binary and Janus compositions, shown in Fig. S2 and S3 of the SI, are compared to estimate the choice of U = 2 eV.

Due to the lack of mirror symmetry, Janus exhibits characteristics distinct from those of a binary. One of these unique features is the intrinsic out-of-plane dipole moment p_z, which induces an internal electric field arising from the difference in electronegativity between X and Y in the up and down layers.[60,61] Investigation of binary $Cr_2X_2Se_2$ monolayers reveals nearly zero out-of-plane dipole moment, as required by their mirror symmetry. The structural asymmetry of the Janus Cr_2XYSe_2 monolayers results in a finite out-of-plane dipole moment, p_z, reported in Table 2. These systems show dipole moments along the z-direction. For most of the monolayers considered, the out-of-plane dipole p_z increases slightly with U. This can be attributed to reduced screening and to enhanced charge asymmetry between the two halogen atoms, X and Y, due to on-site Coulomb interactions. The maximum magnitude of p_z is predicted for Cr_2ClISe_2, which can be related to its larger electronegativity difference compared with Cr_2BrISe_2 and $Cr_2BrClSe_2$. This prediction is consistent with reports indicating that p_z increases with increasing electronegativity, as reported in ref. 62. Although Cr_2BrFSe_2 contains the element with the highest electronegativity, its p_z remains relatively small, suggesting that both structural and electronic effects, such as hybridization near the Fermi level, can partially screen out-of-plane polarization, as shown in Fig. 2.

Table 2 Calculated out-of-plane dipole moment p_z (in Debye) of Janus Cr_2XYSe_2 monolayers as a function of the Hubbard parameter U (in eV)

	p_z (Debye)				
	U = 0	U = 1	U = 2	U = 3	U = 4
Cr_2BrFSe_2	+0.19	+0.18	+0.18	+0.17	+0.15
$Cr_2BrClSe_2$	+0.13	+0.13	+0.14	+0.14	+0.14
Cr_2ClISe_2	−0.32	−0.34	−0.34	−0.36	−0.37
Cr_2BrISe_2	−0.22	−0.21	−0.22	−0.22	−0.23

The sign indicates the dipole's orientation along the z-axis.

B. Magnetic properties and temperature-dependent magnetization

According to DFT+U calculations, all Cr_2XYSe_2 monolayers show the FM ground state at $U \leq 4$ eV. The total magnetic moment per Cr atom is approximately $3\mu_B$ for both binary and Janus systems, while it slightly increases to about $3.27\mu_B$ for $Cr_2F_2Se_2$. The spin parameters J_1, J_2, J_3, A, and δ are derived from the total energy differences between various magnetic

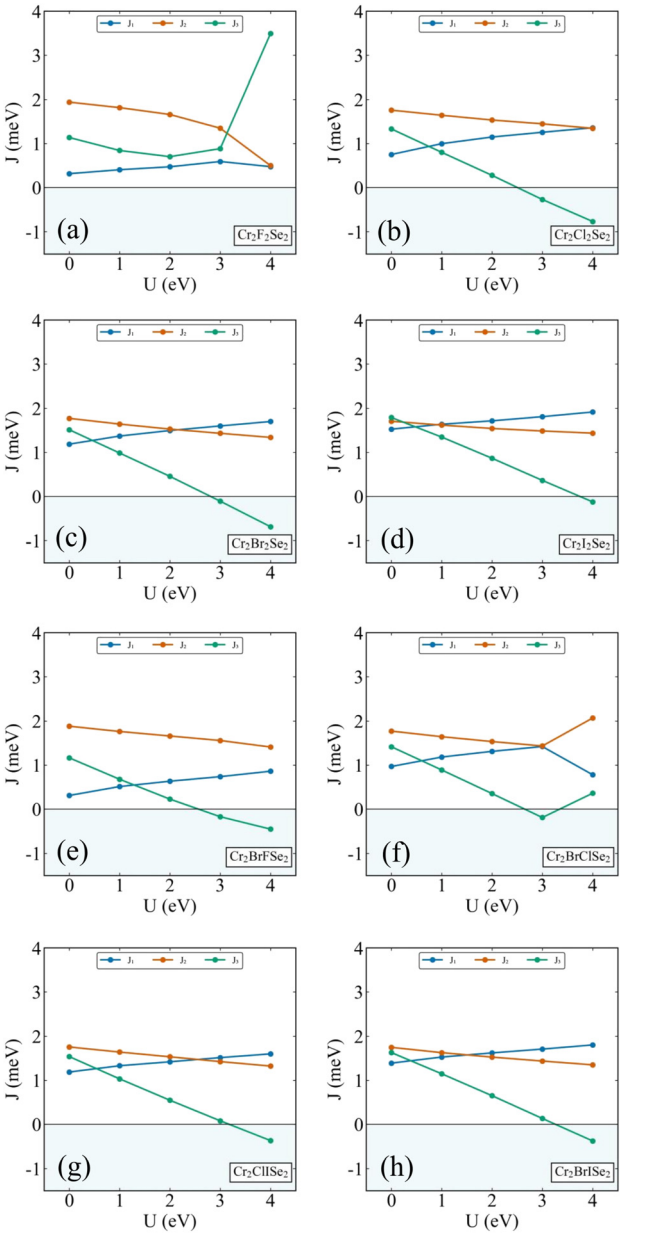

Fig. 3 Variation of the magnetic exchange parameters J_1, J_2, and J_3 (in meV) as a function of the on-site Hubbard interaction U (in eV) for different Cr-based monolayer systems. Panels (a–d) correspond to the binary compounds $Cr_2X_2Se_2$ with X = F, Cl, Br, and I, respectively, while panels (e–h) show the Janus structures Cr_2BrXSe_2 with X = F, Cl, I, and Br, respectively.

configurations. The total energy of each spin configuration was obtained from noncollinear DFT+U calculations.

Fig. 3 presents the variation of the exchange parameters as a function of the Hubbard U parameter for each Cr_2XYSe_2 composition. Notably, the magnitudes of the three different exchange interaction parameters are of the same order of magnitude. In all systems, the exchange interactions between the first- and second-nearest Cr atoms (J_1 and J_2) are positive, favoring ferromagnetic coupling. At the same time, J_3 becomes negative at higher U values in some compounds, indicating a preference toward antiferromagnetic alignment between the third-nearest Cr atoms. As shown in Fig. 3, the value of J_1 increases with U, ranging from approximately 0 to 3 meV, except for $Cr_2F_2Se_2$, which exhibits noticeably lower values of J_1 compared to the other compounds. This drop may be attributed to its smaller lattice parameter a, which further decreases with increasing U, as reported in Table 1. In addition, for $Cr_2F_2Se_2$, the magnitude of J_1 remains smaller than that of J_2 and J_3. The J_2 parameter gradually decreases from about 3 meV as U increases from 0 to 4 eV, indicating a weakening of the next-nearest ferromagnetic channel with enhanced electron localization. An exception is observed in $Cr_2BrClSe_2$, where for $U > 3$ eV the magnitude of J_1 decreases while J_2 increases, suggesting competition between the two exchange interactions. The magnitude of J_3 decreases as U increases in almost all chemical compositions. Besides, the investigation in J_3 shows that the sign is negative in some U values, in favor of the antiparallel spin configuration between the Cr atoms, which interact in the third nearest neighbor separated by distance b. This behavior occurs when the electronic structure of the system changes to a metallic phase (as depicted in Fig. 2). When the system becomes metallic, the exchange mechanism is no longer governed only by localized superexchange. Here, partially itinerant charge carriers at the Fermi level mediate an indirect exchange coupling between localized magnetic atoms *via* Ruderman–Kittel–Kasuya–Yosida (RKKY) interactions between distant Cr moments.[32] The spin polarization of these conduction electrons oscillates with the distance between the magnetic moments. Therefore, depending on the bond distance, it may be ferromagnetic or antiferromagnetic. Consistent with this theory, J_3 decreases with increasing U and becomes negative in the metallic phase, indicating that the RKKY interaction favors an antiparallel alignment between third-nearest-neighbour Cr ions separated by distance b. With decreasing halogen electronegativity from $Cr_2F_2Se_2$ to $Cr_2I_2Se_2$ in the binary systems and from Cr_2BrFSe_2 to Cr_2BrISe_2 in the Janus systems, J_2 and J_3 generally decrease as the lattice constant increases. This behavior is consistent with the reduction of the hopping integral (t) with increasing Cr–Cr distance, leading to a weaker exchange interaction: $J \propto -t^2/U$, where U is the Coulomb energy.[32] However, this trend is not observed for J_1, which increases due to enhanced orbital hybridization arising from the reduced structural symmetry. Consequently, the competition among J_1, J_2, and J_3 determines the strength and stability of the ferromagnetic ordering.

The values of single-ion anisotropy (A) and inter-site magnetic anisotropy (δ) are studied as functions of the Hubbard parameter U for all monolayers, as shown in Fig. 4. The left vertical axis corresponds to A, where positive and negative values indicate the easy axis of magnetization out-of-plane and in-plane, respectively. Since the inter-site anisotropy δ is required only for the in-plane case ($A < 0$), its magnitudes are highlighted in green for the corresponding U values and are represented on the right axis.

For different values of U, the easy axis of magnetization in several monolayers reverses from in-plane to out-of-plane,

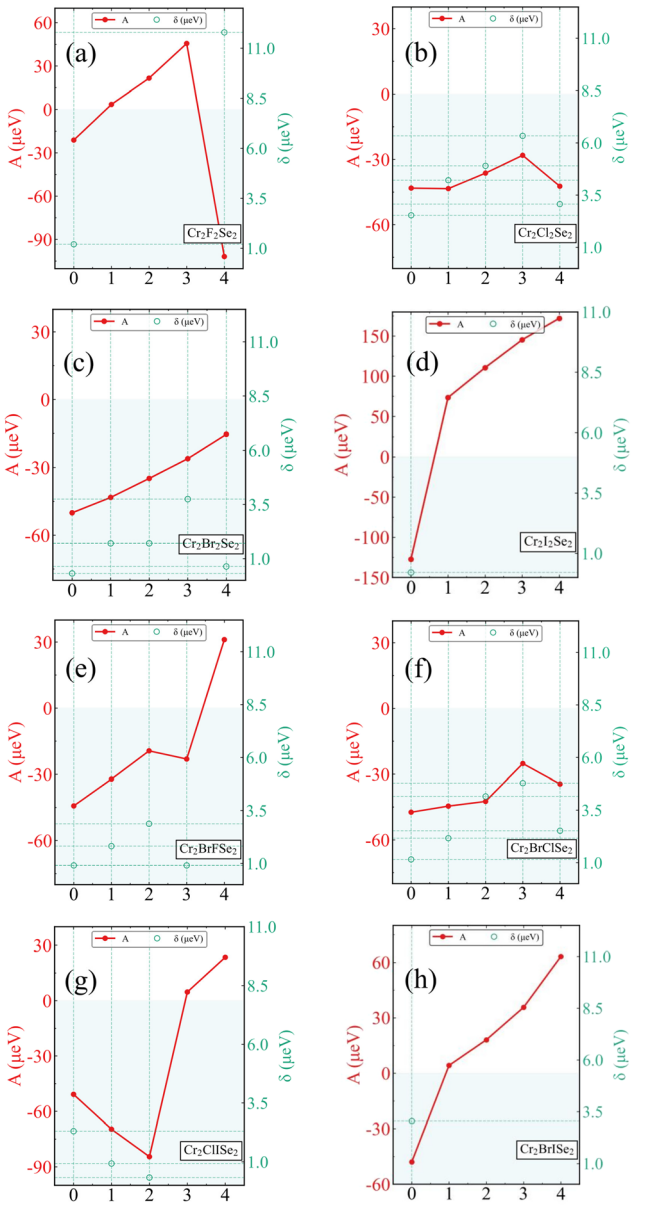

Fig. 4 Variation of the magnetic anisotropy energies, A (left axis, red) and the δ (right axis, teal) as a function of the on-site Hubbard parameter U (in eV) for Cr-based monolayer systems. Panels (a–d) correspond to the binary compounds $Cr_2X_2Se_2$ with X = F, Cl, Br, and I, respectively, while panels (e–h) represent the Janus structures Cr_2BrXSe_2 with X = F, Cl, I, and Br, respectively.

indicating that the magnetic anisotropy is sensitive to the electron correlation strength. In systems containing heavy halogens such as iodine (Fig. 4(d)), strong spin–orbit coupling favors magneto-crystalline anisotropy, stabilizing an out-of-plane easy axis. Correspondingly, the largest single-ion anisotropy values occur in $Cr_2I_2Se_2$ (−100 to 150 μeV) and Cr_2ClISe_2 (−100 to 30 μeV), reflecting the significant spin–orbit interaction introduced by iodine. In Janus structures, the interplay between the out-of-plane asymmetry and spin–orbit coupling contributes to the magnitude of single-ion anisotropy.[62] As seen from Table 2 and Fig. 4, Cr_2ClISe_2 exhibits the largest magnetic anisotropy energy, consistent with its enhanced out-of-plane dipole moment.

This behavior arises from changes in the localization of Cr 3d orbitals and the competition between crystal-field splitting

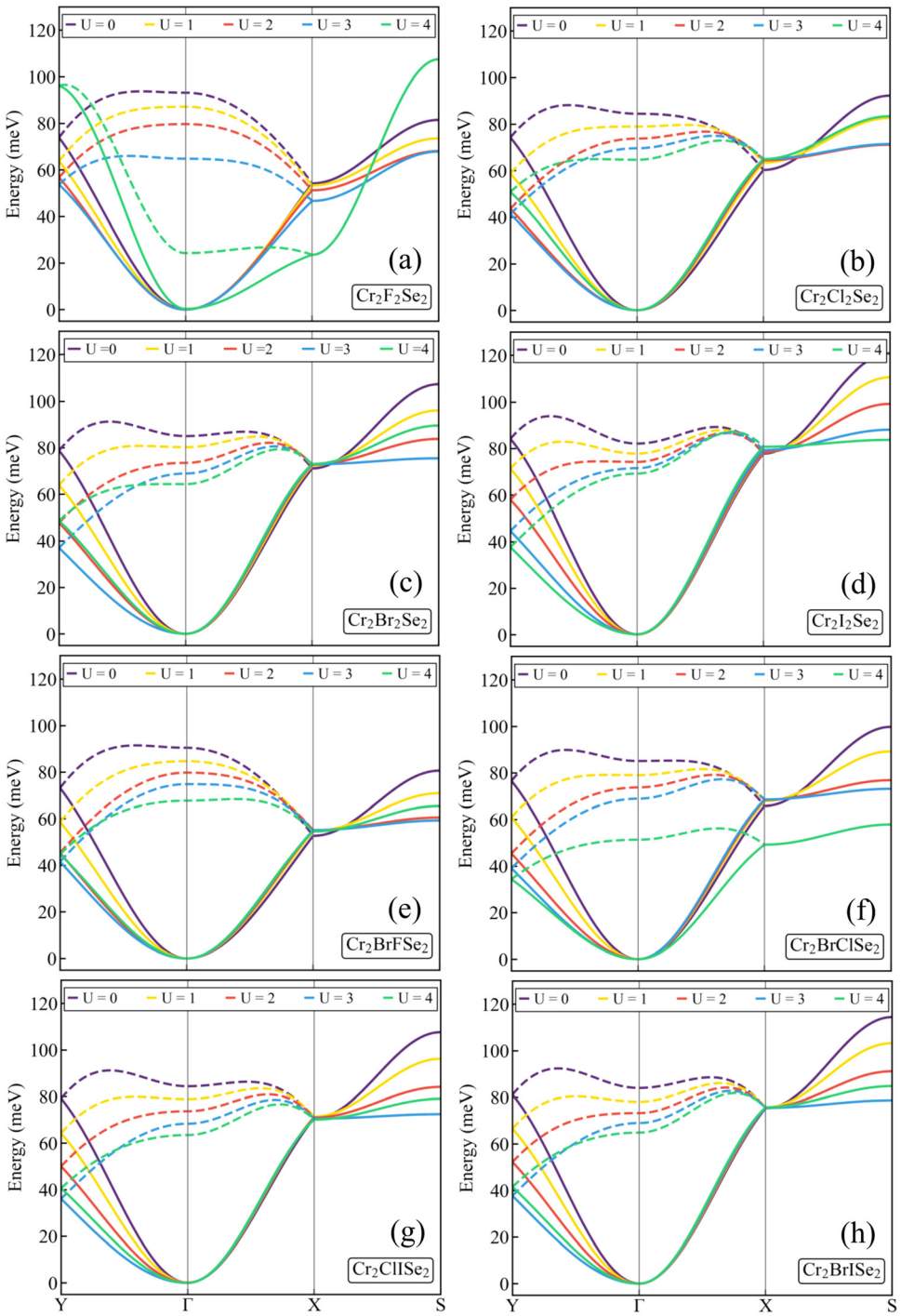

Fig. 5 Magnon dispersion relations along the high-symmetry path Y–Γ–X–S for Cr-based monolayer systems at different on-site Hubbard interaction strengths U (0–4 eV). Panels (a–d) correspond to the binary compounds $Cr_2X_2Se_2$ (X = F, Cl, Br, I), while panels (e–h) show the Janus structures Cr_2BrXSe_2 (X = F, Cl, I, Br). Solid lines represent the acoustic magnon branches, whereas dashed lines denote optical branches.

Table 3 Calculated magnon gap at the Γ point (in meV) as a function of the Hubbard parameter U (eV) for binary and Janus Cr_2XYSe_2 monolayers

Material	$U = 0$	$U = 1$	$U = 2$	$U = 3$	$U = 4$
$Cr_2F_2Se_2$	0.06	0.01	0.03	0.07	0.37
$Cr_2Cl_2Se_2$	0.11	0.14	0.14	0.16	0.12
$Cr_2Br_2Se_2$	0.09	0.10	0.08	0.11	0.04
$Cr_2I_2Se_2$	0.23	0.11	0.16	0.22	0.26
Cr_2BrFSe_2	0.09	0.08	0.08	0.05	0.05
$Cr_2BrClSe_2$	0.10	0.11	0.14	0.12	0.10
Cr_2ClISe_2	0.12	0.14	0.16	0.01	0.03
Cr_2BrISe_2	0.13	0.01	0.03	0.05	0.09

and spin–orbit coupling, which together determine the preferred orientation of the magnetic moments,[2,10] as discussed in the following. To clarify the orbital origin of the easy-axis reorientation, we consider the perturbative contribution of the SOC Hamiltonian,[24] as depicted for $Cr_2F_2Se_2$, $Cr_2I_2Se_2$, Cr_2BrFSe_2, Cr_2ClISe_2, and Cr_2BrISe_2, as shown in Fig. S10–S14 of the SI. The U-induced reorientation of the magnetic easy axis originates from a redistribution of the orbital-resolved SOC matrix elements near the Fermi level. Changing U enhances the localization of the Cr 3d states and modifies their relative energy separation and hybridization with ligand p orbitals. As a representative case, in $Cr_2F_2Se_2$, the dominant contribution at $U = 0$ eV arises from the Cr $d_{x^2-y^2}$–$d_{xy/yz}$ coupling together with Se p_x–p_y states, favoring in-plane anisotropy. When U increases to 1 eV, the spectral weight shifts toward the Cr d_{xz}–d_{z^2} and d_{xy}–d_{yz} channels, accompanied by a change in the Se contribution from p_x–p_y to p_x–p_z, which enhances the matrix elements and drives the transition to out-of-plane magnetization. More details of each composition are available in the SI. To further understand the effect of crystal-field splitting, the partial density of states (PDOS) of the d orbital of Cr atoms is presented in Fig. S5 and S6 of the SI. Because of the low-symmetry orthorhombic structure and the significant hybridization between Cr d orbitals and ligand p states, the Cr 3d bands become fully nondegenerate. As a result, the conventional crystal-field picture with well-defined t_{2g} and e_g splitting is no longer practical.[24,63] Additionally, the largest orbital moments calculated along $L_\parallel$ and $L_\perp$ are reported in Tables VI and VII of the SI. It is well established that the magneto-crystalline anisotropy energy is determined by spin–orbit coupling interactions rather than by the magnitude of the orbital moments. Therefore, the magnetic easy axis can switch to the out-of-plane direction even in the absence of orbital moment reversal.

The magnitude of the inter-site anisotropy, δ, is considerably lower compared with the single-ion anisotropy A, but it plays an essential role in opening the magnon gap at the Γ point of the BZ and in stabilizing long-range magnetization at finite temperature for systems with in-plane magnetization. As shown in Fig. 4(a), the relatively large δ values in $Cr_2F_2Se_2$ (approximately 12 μeV) associated with lighter halogens indicate more substantial anisotropy within the plane, which can be attributed to the enhanced in-plane crystal-field anisotropy. The variations in magnetic parameters with U show the significant effect of electronic correlation on exchange interactions and magneto-crystalline anisotropy.[16,64]

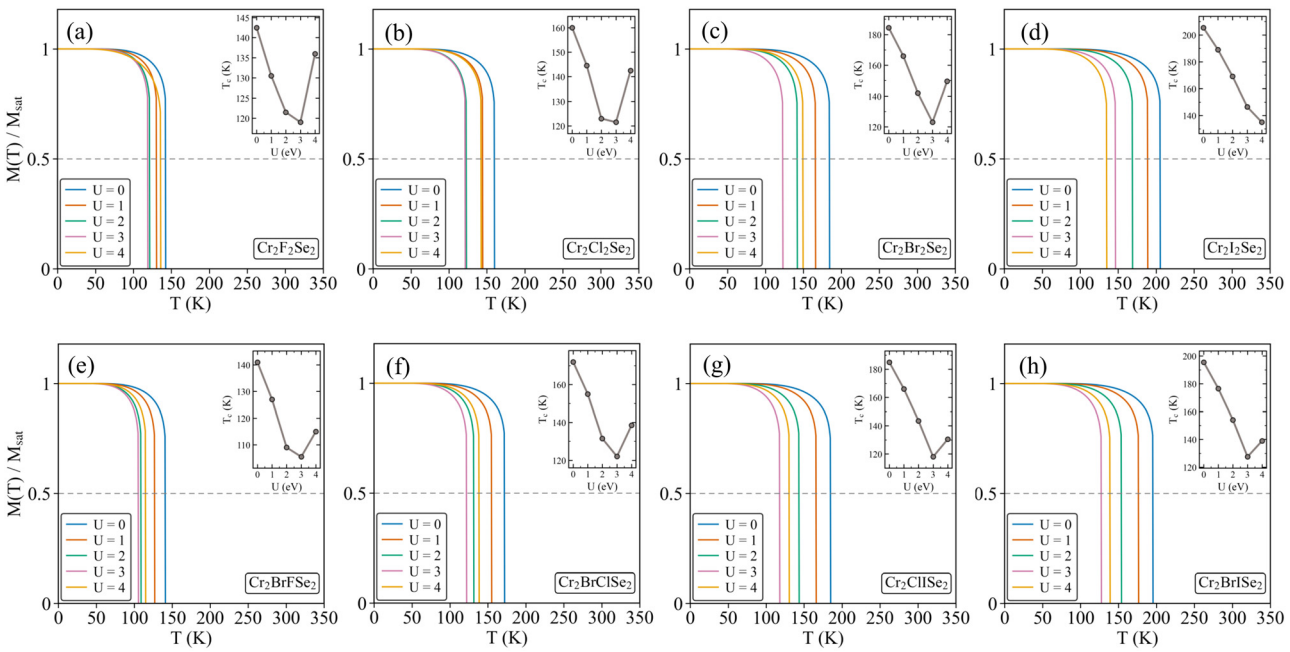

Fig. 6 Temperature-dependent normalized magnetization and corresponding Curie temperatures for various chromium-based monolayers. (a–h) Normalized magnetization $M(T)/M_{sat}$ as a function of temperature T (in K) for (a) $Cr_2F_2Se_2$, (b) $Cr_2Cl_2Se_2$, (c) $Cr_2Br_2Se_2$, (d) $Cr_2I_2Se_2$, (e) Cr_2BrFSe_2, (f) $Cr_2BrClSe_2$, (g) Cr_2ClISe_2, and (h) Cr_2BrISe_2. The different colored curves represent calculations performed with varying values of the Hubbard U parameter from 0 to 4 eV. The dashed horizontal line indicates $M(T)/M_{sat} = 0.5$. The insets show the extracted Curie temperature T_c (in K) as a function of the Hubbard U parameter for each corresponding system.

By using the HP transformation, the magnon dispersion is obtained using eqn (9) and (17) for the monolayers with out-of-plane and in-plane anisotropy, respectively. The corresponding magnon spectra for different materials over the U range are presented in Fig. 5, where acoustic and optical branches emerge due to the two sublattices of the orthorhombic structure. In almost all cases, the magnon energy exhibits a monotonic decrease with increasing Hubbard parameter U, approaching $\sim$100 meV, in good agreement with previous studies.[16] Although the magnon dispersion differs along the Y$-\Gamma$ and $\Gamma-$X directions, it exhibits a quadratic behavior near the Γ point, which is characteristic of ferromagnets. The magnon band of $Cr_2F_2Se_2$ at U = 4 eV differs from the systematic trend observed across all materials and U values. This variation may arise from the distinct behavior of its exchange parameters, illustrated in Fig. 3(a), and the comparatively large magnitude of J_3. The magnon gap at the Γ point is summarized in Table 3. The gap varies significantly with the Hubbard parameter, reflecting the strong U-dependence of the magnetic anisotropy parameters A and δ. Because the magnon dispersion changes with U in the Cr_2XYSe_2 monolayer, the results indicate that electron correlation can play a nontrivial role in their thermodynamic behavior.

The thermal magnetization of the monolayers as a function of the Hubbard parameter U is shown in Fig. 6. As shown in the figure, the magnitude of T_C decreases with increasing U in almost all cases, consistent with the behavior reported in ref. 16. The highest T_C (approximately 200 K) is obtained for $Cr_2I_2Se_2$, consistent with Fig. 3(a), where this compound exhibits the strongest exchange interactions. In contrast, the minimum value of T_C belongs to $Cr_2F_2Se_2$, which shows the weakest exchange interactions and the smallest spin–orbit coupling due to the light fluorine atoms. To demonstrate the reliability of the above predictions, AIMD simulations show no structural reconstruction or bond instability in either binary or Janus Cr_2XYSe_2 monolayers, as shown in Fig. S8 and S9 of the SI. The total energy fluctuations remain below $\sim$40 meV per atom, confirming thermal stability at the transition temperature at the Hubbard parameter U = 2 eV.

IV. Conclusion

We have investigated the structural, electronic, and magnetic properties of orthorhombic Cr_2XYSe_2 (X, Y = F, Cl, Br, I) monolayers using density functional theory and linear spin-wave analysis, focusing on halogen-engineered families. DFPT phonon calculations show that eight of the ten possible binary and Janus structures are dynamically stable in the *Pmmn* phase. For all stable compounds, DFT+U predicts ferromagnetic ground states with magnetic moments close to $3\mu_B$ per Cr atom and electronic properties that vary with both chemical composition and the on-site Coulomb interaction. The calculated exchange interactions and magnetic anisotropies depend on the halogen atoms and U, leading to composition-dependent trends in their magnitudes and orientations. Linear spin-wave theory yields finite magnon gaps at the Γ point for all systems, demonstrating that magnetic anisotropy is required to stabilize long-range magnetic order in 2D Cr_2XYSe_2. The renormalized magnon spectrum causes Curie temperatures of up to approximately 200 K in iodine-based monolayers, representing the maximum thermal stability across the studied compositions.

This work establishes a comprehensive understanding of magnetism in Cr_2XYSe_2 monolayers, which are a tunable family of two-dimensional orthorhombic magnets. The symmetry reduction, chemical substitution, and electron correlation present in these monolayers provide effective control over exchange interactions, magnetic anisotropy, and thermal stability. These findings emphasize the potential of this material class for applications in 2D spintronics and magnonics.

Conflicts of interest

There are no conflicts to declare.

Data availability

The data that support the findings of this study are available within the article and its supplementary information files. Additional data are available from the corresponding author upon reasonable request.

Supplementary information (SI) provides additional details on the following: (1) Phonon dispersion spectra of the stable and unstable monolayers; (2) Heyd–Scuseria–Ernzerhof (HSE06) hybrid functional band structure calculations to validate the Hubbard parameter; (3) Different out-of-plane antiferromagnetic spin configurations; (4) Analytical formalism for the anisotropic Heisenberg model and spin-wave excitations; (5) Calculated Cr–Cr bond distances and Bader charges summarized in tables; (6) Full spin-polarized electronic band structures and partial density of states (PDOS); (7) *Ab initio* molecular dynamics (AIMD) simulation results; and (8) Analysis of orbital-projected spin–orbit coupling (SOC) and magneto-crystalline anisotropy energy (MAE). See DOI: https://doi.org/10.1039/d5cp04913j.

Acknowledgements

This work was supported by the FLAG-ERA grant MNEMOSYN and by the Scientific and Technological Research Council of Türkiye (TUBITAK) under project no. 221N400. The numerical calculations reported in this paper were partially performed at TUBITAK ULAKBIM, High Performance and Grid Computing Center (TRUBA resources). Y. Mogulkoc acknowledges The Turkish Academy of Sciences – Outstanding Young Scientists Award Program (TUBA-GEBIP) for partial funding of this research.

References

1 K. S. Burch, D. Mandrus and J.-G. Park, Magnetism in two-dimensional van der Waals materials, *Nature*, 2018, **563**, 47.

2 J. L. Lado and J. Fernández-Rossier, On the origin of magnetic anisotropy in two dimensional CrI_3, *2D Mater.*, 2017, **4**, 035002.
3 B. Huang, G. Clark, E. Navarro-Moratalla, D. R. Klein, R. Cheng, K. L. Seyler, D. Zhong, E. Schmidgall, M. A. McGuire and D. H. Cobden, *et al.*, Layer-dependent ferromagnetism in a van der Waals crystal down to the monolayer limit, *Nature*, 2017, **546**, 270.
4 C. Gong, L. Li, Z. Li, H. Ji, A. Stern, Y. Xia, T. Cao, W. Bao, C. Wang and Y. Wang, *et al.*, Discovery of intrinsic ferromagnetism in two-dimensional van der Waals crystals, *Nature*, 2017, **546**, 265.
5 Z. Fei, B. Huang, P. Malinowski, W. Wang, T. Song, J. Sanchez, W. Yao, D. Xiao, X. Zhu and A. F. May, *et al.*, Two-dimensional itinerant ferromagnetism in atomically thin Fe_3GeTe_2, *Nat. Mater.*, 2018, **17**, 778.
6 A. F. May, D. Ovchinnikov, Q. Zheng, R. Hermann, S. Calder, B. Huang, Z. Fei, Y. Liu, X. Xu and M. A. McGuire, Ferromagnetism near room temperature in the cleavable van der Waals crystal Fe_5GeTe_2, *ACS Nano*, 2019, **13**, 4436.
7 F. Han, X. Yan, A. Bergara, W. Li, H. Yu and G. Yang, A Janus CrSSe monolayer with interesting ferromagnetism, *Phys. Chem. Chem. Phys.*, 2023, **25**, 29672.
8 E. J. Telford, A. H. Dismukes, K. Lee, M. Cheng, A. Wieteska, A. K. Bartholomew, Y.-S. Chen, X. Xu, A. N. Pasupathy and X. Zhu, *et al.*, Layered antiferromagnetism induces large negative magnetoresistance in the van der Waals semiconductor CrSBr, *Adv. Mater.*, 2020, **32**, 2003240.
9 K. F. Mak, J. Shan and D. C. Ralph, Probing and controlling magnetic states in 2D layered magnetic materials, *Nat. Rev. Phys.*, 2019, **1**, 646.
10 Y. Hou and R. Wu, Magnetic anisotropy in 2D van der Waals magnetic materials and their heterostructures: importance, mechanisms, and opportunities, *Adv. Funct. Mater.*, 2025, e09453.
11 S. Memarzadeh, M. R. Roknabadi, M. Modarresi, A. Mogulkoc and A. Rudenko, Role of charge doping and strain in the stabilization of in-plane ferromagnetism in monolayer VSe_2 at room temperature, *2D Mater.*, 2021, **8**, 035022.
12 S. D. Tanha, M. Modarresi, M. Roknabadi, T. Hu and A. Mogulkoc, The antiferromagnetic phase of a Wurtzite nickel sulfide monolayer, *Phys. Chem. Chem. Phys.*, 2024, **26**, 22403.
13 Z. Guan, Z. Shen, Y. Xue, T. Zhong, X. Wu and C. Song, Electronic properties, skyrmions and bimerons in Janus CrXY (X, Y = S, Se, Te, Cl, Br, I, and X $\neq$ Y) monolayers, *Phys. Chem. Chem. Phys.*, 2023, **25**, 24968.
14 D. Zhang, Z. Yang, T. Wu, W. Ji and Y. Zhang, Switchable magnetic and electronic properties in CrSX (X = Cl, Br, I) monolayers, *Phys. Rev. Mater.*, 2025, **9**, 054004.
15 K. Lee, A. H. Dismukes, E. J. Telford, R. A. Wiscons, J. Wang, X. Xu, C. Nuckolls, C. R. Dean, X. Roy and X. Zhu, Magnetic order and symmetry in the 2D semiconductor CrSBr, *Nano Lett.*, 2021, **21**, 3511.
16 A. N. Rudenko, M. Rösner and M. I. Katsnelson, Dielectric tunability of magnetic properties in orthorhombic ferromagnetic monolayer CrSBr, *npj Comput. Mater.*, 2023, **9**, 83.
17 R. Han and Y. Yan, Strain-tunable electric structure and magnetic anisotropy in monolayer CrSi, *Phys. Chem. Chem. Phys.*, 2019, **21**, 20892.
18 S. Chen, F. Wu, Q. Li, H. Sun, J. Ding, C. Huang and E. Kan, Prediction of room-temperature ferromagnetism in a two-dimensional direct band gap semiconductor, *Nanoscale*, 2020, **12**, 15670.
19 R. Han, H. Hou, X. Xue and Y. Yan, Enhancement of perpendicular magnetic anisotropy and Curie temperature in V-doped two-dimensional CrSi Janus semiconductor monolayer, *J. Phys. Chem. C*, 2023, **127**, 2003.
20 R. Han, H. Hou and Y. Yan, Large perpendicular magnetic anisotropy, high Curie temperature, and halfmetallicity in monolayer CrSi induced by substitution doping, *J. Magn. Magn. Mater.*, 2023, **584**, 171074.
21 H. Wang, J. Qi and X. Qian, Electrically tunable high Curie temperature two-dimensional ferromagnetism in van der Waals layered crystals, *Appl. Phys. Lett.*, 2020, **117**, 083102, DOI: 10.1063/5.0014865.
22 B. Xu, S. Li, K. Jiang, J. Yin, Z. Liu, Y. Cheng and W. Zhong, Switching of the magnetic anisotropy via strain in two dimensional multiferroic materials: CrSX (X = Cl, Br, I), *Appl. Phys. Lett.*, 2020, **116**, 052403, DOI: 10.1063/1.5140644.
23 Y. Diao, C. Jin, X. Gu, Z. Lu, J. Zhang, Z. Dong, D. Liu, H. Fu and C. Zhong, Strain-regulated magnetic phase transition and perpendicular magnetic anisotropy in CrSBr monolayer, *Phys. E*, 2023, **147**, 115590.
24 R. Han, X. Xue and P. Li, Enhanced ferromagnetism, perpendicular magnetic anisotropy and high Curie temperature in the van der Waals semiconductor crsebr through strain and doping, *Phys. Chem. Chem. Phys.*, 2024, **26**, 12219.
25 N. P. Wilson, K. Lee, J. Cenker, K. Xie, A. H. Dismukes, E. J. Telford, J. Fonseca, S. Sivakumar, C. Dean and T. Cao, *et al.*, Interlayer electronic coupling on demand in a 2D magnetic semiconductor, *Nat. Mater.*, 2021, **20**, 1657.
26 F. Wu, I. Gutiérrez-Lezama, S. A. López-Paz, M. Gibertini, K. Watanabe, T. Taniguchi, F. O. von Rohr, N. Ubrig and A. F. Morpurgo, Quasi-1D electronic transport in a 2D magnetic semiconductor, *Adv. Mater.*, 2022, **34**, 2109759.
27 C. Boix-Constant, S. Mañas-Valero, A. M. Ruiz, A. Rybakov, K. A. Konieczny, S. Pillet, J. J. Baldoví and E. Coronado, Probing the spin dimensionality in single-layer CrSBr van der Waals heterostructures by magneto-transport measurements, *Adv. Mater.*, 2022, **34**, 2204940.
28 J. Klein, B. Pingault, M. Florian, M.-C. Heißenbüttel, A. Steinhoff, Z. Song, K. Torres, F. Dirnberger, J. B. Curtis and M. Weile, *et al.*, The bulk van der Waals layered magnet CrSBr is a quasi-1D material, *ACS Nano*, 2023, **17**(6), 5316–5328, DOI: 10.1021/acsnano.2c07316.
29 J. Jiang and W. Mi, Two-dimensional magnetic Janus monolayers and their van der Waals heterostructures: a review on recent progress, *Mater. Horiz.*, 2023, **10**, 788.
30 X. Bo, F. Li, X. Xu, X. Wan and Y. Pu, Calculated magnetic exchange interactions in the van der Waals layered magnet CrSBr, *New J. Phys.*, 2023, **25**, 013026.

31 E. J. Telford, A. H. Dismukes, R. L. Dudley, R. A. Wiscons, K. Lee, D. G. Chica, M. E. Ziebel, M.-G. Han, J. Yu and S. Shabani, *et al.*, Coupling between magnetic order and charge transport in a two-dimensional magnetic semiconductor, *Nat. Mater.*, 2022, **21**, 754.
32 S. Blundell, *Magnetism in condensed matter*, OUP, Oxford, 2001.
33 N. Majlis, *The quantum theory of magnetism*, World Scientific, 2007.
34 D. L. Esteras, A. Rybakov, A. M. Ruiz and J. J. Baldoví, Magnon straintronics in the 2D van der Waals ferromagnet CrSBr from first-principles, *Nano Lett.*, 2022, **22**, 8771.
35 L. Han, Z. Li, Z. Tang, X. Wang, J. Li, C. He, C. Tang and T. Ouyang, Notable impact of magnetic order and flat phonon mode on the thermal transport properties of 2D magnetic semiconductor CrSBr, *J. Appl. Phys.*, 2025, **138**, 195101, DOI: 10.1063/5.0270732.
36 P. E. Blöchl, Projector augmented-wave method, *Phys. Rev. B: Condens. Matter Mater. Phys.*, 1994, **50**, 17953.
37 G. Kresse and D. Joubert, From ultrasoft pseudopotentials to the projector augmented-wave method, *Phys. Rev. B: Condens. Matter Mater. Phys.*, 1999, **59**, 1758.
38 G. Kresse and J. Furthmüller, Efficiency of ab initio total energy calculations for metals and semiconductors using a plane-wave basis set, *Comput. Mater. Sci.*, 1996, **6**, 15.
39 G. Kresse and J. Furthmüller, Efficient iterative schemes for ab initio total-energy calculations using a plane-wave basis set, *Phys. Rev. B: Condens. Matter Mater. Phys.*, 1996, **54**, 11169.
40 J. P. Perdew, K. Burke and M. Ernzerhof, Generalized gradient approximation made simple, *Phys. Rev. Lett.*, 1996, **77**, 3865.
41 V. I. Anisimov, F. Aryasetiawan and A. Lichtenstein, First-principles calculations of the electronic structure and spectra of strongly correlated systems: the LDA+U method, *J. Phys.: Condens. Matter*, 1997, **9**, 767.
42 S. L. Dudarev, G. A. Botton, S. Y. Savrasov, C. Humphreys and A. P. Sutton, Electron-energy-loss spectra and the structural stability of nickel oxide: an LSDA+U study, *Phys. Rev. B: Condens. Matter Mater. Phys.*, 1998, **57**, 1505.
43 J. Heyd, G. E. Scuseria and M. Ernzerhof, Hybrid functionals based on a screened coulomb potential, *J. Chem. Phys.*, 2003, **118**, 8207.
44 A. V. Krukau, O. A. Vydrov, A. F. Izmaylov and G. E. Scuseria, Influence of the exchange screening parameter on the performance of screened hybrid functionals, *J. Chem. Phys.*, 2006, **125**, 224106, DOI: 10.1063/1.2404663.
45 H. J. Monkhorst and J. D. Pack, Special points for Brillouin-zone integrations, *Phys. Rev. B: Condens. Matter Mater. Phys.*, 1976, **13**, 5188.
46 A. Togo and I. Tanaka, First principles phonon calculations in materials science, *Scr. Mater.*, 2015, **108**, 1.
47 H. C. Andersen, Molecular dynamics simulations at constant pressure and/or temperature, *J. Chem. Phys.*, 1980, **72**, 2384.
48 N. Metropolis and S. Ulam, The monte carlo method, *J. Am. Stat. Assoc.*, 1949, **44**, 335.
49 D. N. Zubarev, Double-time green functions in statistical physics, *Soviet Physics Uspekhi*, 1960, **3**, 320.
50 T. Holstein and H. Primakoff, Field dependence of the intrinsic domain magnetization of a ferromagnet, *Phys. Rev.*, 1940, **58**, 1098.
51 S. Tiwari, J. Vanherck, M. L. Van de Put, W. G. Vandenberghe and B. Sorée, Computing Curie temperature of two-dimensional ferromagnets in the presence of exchange anisotropy, *Phy. Rev. Res.*, 2021, **3**, 043024.
52 T. Olsen, Theory and simulations of critical temperatures in CrI_3 and other 2D materials: easy-axis magnetic order and easy-plane kosterlitz–thouless transitions, *MRS Commun.*, 2019, **9**, 1142.
53 N. D. Mermin and H. Wagner, Absence of ferromagnetism or antiferromagnetism in one-or two-dimensional isotropic Heisenberg models, *Phys. Rev. Lett.*, 1966, **17**, 1133.
54 R. Caglayan, Y. Mogulkoc, A. Mogulkoc, M. Modarresi and A. Rudenko, Easy-axis rotation in ferromagnetic monolayer crn induced by fluorine and chlorine functionalization, *Phys. Chem. Chem. Phys.*, 2022, **24**, 25426.
55 R. Caglayan, A. Mogulkoc, Y. Mogulkoc, M. Modarresi and A. Rudenko, Dzyaloshinskii-moriya interaction and nontrivial spin textures in the Janus semiconductor monolayers VXY (X = Cl, Br, I; Y = S, Se, Te), *Phys. Rev. B*, 2024, **110**, 094440.
56 A. Mogulkoc and R. Caglayan, Remarkable dzyaloshinskii-moriya interaction in ferromagnetic SnC/MnSeX (X = Se, Te) heterobilayers, *Phys. Rev. Mater.*, 2025, **9**, 064004.
57 R. Beck, *Examination of Defect-Induced Properties in Nanomaterial Systems*, University of Washington, 2021.
58 D. R. Lide, *CRC handbook of chemistry and physics*, The Chemical Rubber Company, 88th edn, 2008.
59 A. V. Bondi, van der Waals volumes and radii, *J. Phys. Chem.*, 1964, **68**, 441.
60 J.-C. Lian, W.-Q. Huang, W. Hu and G.-F. Huang, Electrostatic potential anomaly in 2D Janus transition metal dichalcogenides, *Ann. Phys.*, 2019, **531**, 1900369.
61 W.-J. Yin, H.-J. Tan, P.-J. Ding, B. Wen, X.-B. Li, G. Teobaldi and L.-M. Liu, Recent advances in lowdimensional Janus materials: theoretical and simulation perspectives, *Mater. Adv.*, 2021, **2**, 7543.
62 M. Azmoonfar, M. Roknabadi, M. Modarresi and A. Mogulkoc, Characterization of two dimensional ferromagnetic binary and Janus manganese dichalcogenides, *J. Magn. Magn. Mater.*, 2022, **556**, 169412.
63 E. Maskar, A. F. Lamrani, A. Es-Smairi, A. Louardi, A. Yvaz and D. Rai, Electronic, magnetic, and thermodynamic properties of orthorhombic $CeScO_3$, $CeTiO_3$, and $CeVO_3$ using GGA and GGA+U, *Comput. Condens. Matter*, 2024, **38**, e00873.
64 A. Mogulkoc, M. Modarresi and A. Rudenko, Twodimensional chromium pnictides CrX (X = P, As, Sb): halfmetallic ferromagnets with high Curie temperature, *Phys. Rev. B*, 2020, **102**, 024441.